

Chapter 4

Betatron coupling: Merging Formalisms and Localization of Sources

4.1 Introduction

Betatron coupling in circular accelerators has been widely studied using both matrix formalism and Hamiltonian perturbation theory. In the matrix formalism the transverse beam motion is represented by a 4×4 one-turn matrix \mathbf{T} which can be factorized into a block diagonal normal mode form [41, 42]

$$\mathbf{T} = \begin{pmatrix} \mathbf{M} & \mathbf{m} \\ \mathbf{n} & \mathbf{N} \end{pmatrix} = \mathbf{V}\mathbf{U}\mathbf{V}^{-1} \quad (4.1)$$

by means of the similarity transformation. The symplectic 4×4 matrices \mathbf{U} and \mathbf{V} of the form

$$\mathbf{U} = \begin{pmatrix} \mathbf{A} & \mathbf{0} \\ \mathbf{0} & \mathbf{B} \end{pmatrix}, \quad \mathbf{V} = \begin{pmatrix} \gamma \mathbf{I} & \mathbf{C} \\ -\mathbf{C}^\dagger & \gamma \mathbf{I} \end{pmatrix}, \quad (4.2)$$

consisting of the transverse Twiss functions and a 2×2 coupling matrix (\mathbf{C} matrix) respectively. \mathbf{I} is the 2×2 identity matrix, \mathbf{C} is the 2×2 coupling matrix, and \mathbf{C}^\dagger is its symplectic conjugate requiring

$$|\mathbf{C}| + \gamma^2 = 1. \quad (4.3)$$

Therefore, the parameters γ and \mathbf{C} are given

$$\gamma = \sqrt{\frac{1}{2} + \frac{1}{2} \sqrt{\frac{\text{Tr}[\mathbf{M} - \mathbf{N}]^2}{\text{Tr}[\mathbf{M} - \mathbf{N}]^2 + 4|\mathbf{H}|}}} \quad (4.4)$$

$$\mathbf{C} = \frac{-\mathbf{H} \text{sgn}\{\text{Tr}[\mathbf{M} - \mathbf{N}]\}}{\text{Tr}[\mathbf{M} - \mathbf{N}]^2 + 4|\mathbf{H}|} \quad (4.5)$$

where,

$$\mathbf{H} = \mathbf{m} + \mathbf{n}^\dagger \quad (4.6)$$

For stable motion, it can be shown that

$$\text{Tr}[\mathbf{M} - \mathbf{N}]^2 + 4|\mathbf{H}| > 0. \quad (4.7)$$

In the Hamiltonian approach the coupling elements are considered to be a perturbation to the uncoupled lattice. The perturbed Hamiltonian is given by

$$\mathcal{H} = \mathcal{H}_0 + \mathcal{H}_1 = \frac{1}{2} [p_x^2 + p_y^2 + k_x(s)x^2 + k_y(s)y^2] + p(s)xy \quad (4.8)$$

where $k_x(s) = \rho^2 - \frac{1}{B\rho} \frac{\partial B_x}{\partial y}$, $k_y(s) = \rho^2 - \frac{1}{B\rho} \frac{\partial B_y}{\partial x}$, and $p(s) = \frac{1}{B\rho} \left(\frac{\partial B_x}{\partial x} - \frac{\partial B_y}{\partial y} \right)$. The equations of motion are expanded up to the first order in those perturbations. Direct relations between the two approaches are derived and discussed in detail and their applicability to localize and measure transverse coupling sources are presented.

Numerical methods such as Fourier Transform and Singular Value Decomposition (SVD) have been demonstrated to be effective in measuring relevant quantities in both formalisms [43, 44, 45, 46]. However, in the matrix formalism, measurements have been constrained to three of the four elements in the coupling matrix [44, 45]. The individual elements of the coupling matrix usually have complicated behavior around the ring. One often has to rely on fitting techniques to identify sources of local coupling [44]. An approach to extend the existing methods to measure the complete \mathbf{C} matrix and hence the determinant is presented. The behavior of the determinant in the presence of coupling sources is discussed in detail and its advantage of localizing these coupling sources is transparent. The applicability of the expression relating closest tune approach (ΔQ_{min}) and $\overline{\mathbf{C}}$ matrix given in Refs. [47] and [48] is also studied.

4.2 Hamiltonian terms and coupling matrix

To relate the coupling matrix to the Hamiltonian terms the expressions describing the turn-by-turn motion from both formalisms are compared. This is achieved by introducing the canonical momentum in the matrix framework and constructing a complex variable. Prior to this the two approaches in terms of particle motion are briefly discussed.

4.2.1 Matrix formalism

Since the Twiss parameters are dependent on choice of axis, it is useful to normalize the normal modes with

$$\begin{bmatrix} a \\ a' \\ b \\ b' \end{bmatrix} = \begin{bmatrix} G_a & 0 \\ 0 & G_b \end{bmatrix} \begin{bmatrix} x \\ x' \\ y \\ y' \end{bmatrix} \quad (4.9)$$

By means of this similarity transformation the β dependence is normalized out of \mathbf{C} ,

$$\overline{\mathbf{C}} = \mathbf{G}_a \mathbf{C} \mathbf{G}_b^{-1} \quad (4.10)$$

where

$$\mathbf{G}_{a,b} = \begin{bmatrix} \frac{1}{\sqrt{\beta_{a,b}}} & 0 \\ \frac{\alpha_{a,b}}{\sqrt{\beta_{a,b}}} & \sqrt{\beta_{a,b}} \end{bmatrix} \quad (4.11)$$

are the normalization matrices for the a and b modes [42]. Note that $|\overline{\mathbf{C}}| = |\mathbf{C}|$. The normalized motion in the horizontal and vertical planes can be expressed as

$$\begin{bmatrix} \hat{x} \\ \hat{p}_x \\ \hat{y} \\ \hat{p}_y \end{bmatrix} = \begin{bmatrix} \gamma & 0 & \overline{C}_{11} & \overline{C}_{12} \\ 0 & \gamma & \overline{C}_{21} & \overline{C}_{22} \\ -\overline{C}_{22} & \overline{C}_{12} & \gamma & 0 \\ \overline{C}_{21} & -\overline{C}_{11} & 0 & \gamma \end{bmatrix} \begin{bmatrix} A_x C \psi_x \\ A_x S \psi_x \\ A_y C \psi_y \\ A_y S \psi_y \end{bmatrix} \quad (4.12)$$

where “ C ” and “ S ” are the cosine and sine functions respectively. Using the above expressions for normalized positions and momenta, the complex variables are given by

$$\hat{x} + i\hat{p}_x = \gamma A_x e^{i\psi_x} \quad (4.13)$$

$$\begin{aligned} & + \frac{A_y}{2} \left((\overline{C}_{11} + i\overline{C}_{12} + i\overline{C}_{21} - \overline{C}_{22}) e^{-i\psi_y} \right. \\ & \left. + (\overline{C}_{11} - i\overline{C}_{12} + i\overline{C}_{21} + \overline{C}_{22}) e^{i\psi_y} \right), \\ \hat{y} + i\hat{p}_y &= \gamma A_y e^{i\psi_y} \quad (4.14) \\ & + \frac{A_x}{2} \left((\overline{C}_{11} + i\overline{C}_{12} + i\overline{C}_{21} - \overline{C}_{22}) e^{-i\psi_x} \right. \\ & \left. + (-\overline{C}_{11} - i\overline{C}_{12} + i\overline{C}_{21} - \overline{C}_{22}) e^{i\psi_x} \right). \end{aligned}$$

Note that the convention for momenta used in Hamiltonian theory described in [49] is the negative of that used in matrix formalism described in Ref. [50] ($\hat{p}_x^h = -\hat{p}_x$).

4.2.2 Resonance driving terms

Using Hamiltonian and Normal Form theory a weakly coupled lattice is treated as a perturbation to the uncoupled lattice. The turn-by-turn normalized particle positions and momenta at a location s are described as [49],

$$\hat{x} - i\hat{p}_x^h = \sqrt{2I_x}e^{i\psi_x} - 2if_{1001}\sqrt{2I_y}e^{i\psi_y} - 2if_{1010}\sqrt{2I_y}e^{-i\psi_y}, \quad (4.15)$$

$$\hat{y} - i\hat{p}_y^h = \sqrt{2I_y}e^{i\psi_y} - 2if_{1001}^*\sqrt{2I_x}e^{i\psi_x} - 2if_{1010}\sqrt{2I_x}e^{-i\psi_x}, \quad (4.16)$$

where $I_{x,y}$ are the horizontal and the vertical invariants. The phases of the oscillations, $\psi_{x,y}$ are expressed as function of the natural tunes $Q_{x,y}$, the turn number N and the initial phases $\phi_{x0,y0}$ as $\psi_{x,y} = 2\pi Q_{x,y}N + \phi_{x0,y0}$. The resonance driving terms (RDT's) f_{1001} and f_{1010} are proportional to the Hamiltonian terms [49] and drive the difference and the sum resonances respectively. These terms are functions of the uncoupled lattice parameters at the location of both the coupling elements and the observation point s given by

$$f(s)_{1010}^{1001} = -\frac{1}{4(1 - e^{2\pi i(Q_x \mp Q_y)})} \sum_l k_l \sqrt{\beta_x^l \beta_y^l} e^{i(\Delta\phi_x^{sl} \mp \Delta\phi_y^{sl})} \quad (4.17)$$

where k_l is the l^{th} integrated skew quadrupole strength, $\beta_{x,y}^l$ are the Twiss functions at the location of the l^{th} skew quadrupole, $\Delta\phi_{x,y}^{sl}$ are the phase advances between the observation point s and the l^{th} skew quadrupole and $Q_{x,y}$ are the horizontal and vertical tunes.

4.2.3 Relating the C matrix to RDT's

The relation to the Hamiltonian formalism can now be established by directly comparing Eqs. (4.15) and (4.16) to Eqs. (4.13) and (4.14) obtaining,

$$f_{1001} = \frac{1}{4\gamma}(\overline{C}_{12} - \overline{C}_{21} + i\overline{C}_{11} + i\overline{C}_{22}), \quad (4.18)$$

$$f_{1010} = \frac{1}{4\gamma}(-\overline{C}_{12} - \overline{C}_{21} + i\overline{C}_{11} - i\overline{C}_{22}), \quad (4.19)$$

or, equivalently expressing \overline{C} as function of the RDT's,

$$\frac{1}{2\gamma}\overline{C}_{21}^{12} = -\mathcal{Re}\{f_{1010} \mp f_{1001}\}, \quad (4.20)$$

$$\frac{1}{2\gamma}\overline{C}_{22}^{11} = \mathcal{Im}\{f_{1001} \pm f_{1010}\}, \quad (4.21)$$

where \mathcal{R} and \mathcal{I} stand for real and imaginary parts respectively. The determinant of $\overline{\mathbf{C}}$ can also be related to the RDT's as

$$\frac{|\overline{\mathbf{C}}|}{4\gamma^2} = |f_{1001}|^2 - |f_{1010}|^2, \quad (4.22)$$

and using $|\overline{\mathbf{C}}| + \gamma^2 = 1$ yields,

$$|\overline{\mathbf{C}}| = 1 - \frac{1}{1 + 4(|f_{1001}|^2 - |f_{1010}|^2)}, \quad (4.23)$$

$$\gamma^2 = \frac{1}{1 + 4(|f_{1001}|^2 - |f_{1010}|^2)} \quad (4.24)$$

These expressions have a direct interpretation: if $|\overline{\mathbf{C}}|$ is positive the difference resonance (f_{1001}) dominates, and if it is negative the sum resonance (f_{1010}) dominates. From these expressions it is also observed that a null $|\overline{\mathbf{C}}|$ does not imply null coupling, but $|f_{1001}| = |f_{1010}|$. If $|f_{1010}|^2 > (\frac{1}{4} + |f_{1001}|)$, then $\gamma^2 < 0$ and the particle motion is unstable (see discussion in [42] after Eq. (12)).

In [46] it was demonstrated that the amplitude of the RDT's remains constant along sections free of coupling sources and experiences abrupt jumps at locations with couplers. In [46] it is also shown that the relative longitudinal variations of the RDT's become smaller as the tunes approach the resonance. On the resonance, the amplitude of the RDT's becomes invariant around the ring. Thus, by virtue of Eq. (4.22), the determinant of $\overline{\mathbf{C}}$ also tends to be invariant around the ring as the tunes approach the resonance.

4.2.4 Simulations

To confirm the relations derived above, simulations were carried out with the aid of MAD-X [51]. A simple ring consisting of 80 FODO cells is constructed using parameters shown in Table 4.1. Three skew quadrupoles of

Table 4.1: FODO Lattice Parameters (NA: Not applicable)

Species	Length (m)	Strength
Dipoles	6.5	0.039 rad
Quadrupoles	0.5	0.1 m^{-2}
Skew Quadrupoles	0.2	$4.3 \times 10^{-3} \text{ m}^{-2}$
Drifts	0.25	NA

different strengths were placed at arbitrary locations to introduce transverse coupling in the lattice.

f_{1001} and $\overline{\mathbf{C}}$ matrix

Twiss functions and coupling matrix elements in the form of \mathbf{R} matrix (Edwards-Teng parameterization [41]) are directly available from MAD-X. The \mathbf{C} matrix is determined by a simple transformation of the \mathbf{R} matrix given by

$$\mathbf{C} = \frac{1}{1 + |\mathbf{R}|} \mathbf{J}^{-1} \mathbf{R} \mathbf{J} \quad (4.25)$$

where $\mathbf{J} = \begin{bmatrix} 0 & 1 \\ -1 & 0 \end{bmatrix}$. $\overline{\mathbf{C}}$ is obtained from Eq. (4.10) by normalizing out the beta dependence from \mathbf{C} . To calculate the RDT's f_{1001} and f_{1010} from MAD-X, the first order approximation given by Eq. (4.17) is used. Fig. 4.1

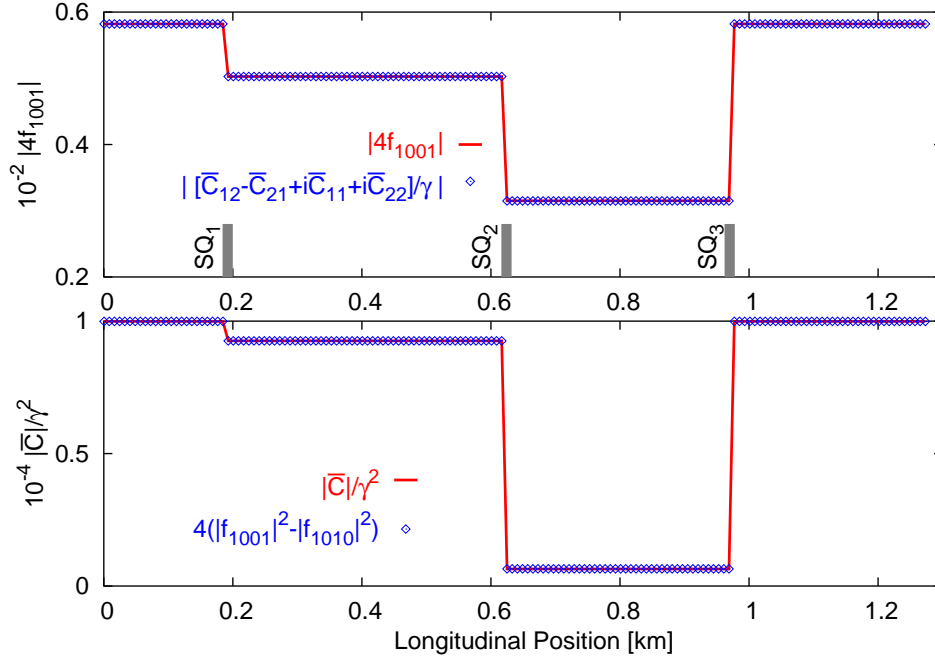


Figure 4.1: Top: $4|f_{1001}|$ and $|[(\overline{C}_{12} - \overline{C}_{21}) + i(\overline{C}_{11} + \overline{C}_{22})]/\gamma|$ plotted as a function of the longitudinal position. Bottom: $|\overline{C}|/\gamma^2$ and $4(|f_{1001}|^2 - |f_{1010}|^2)$ plotted as a function of longitudinal position. Horizontal and vertical tunes are $Q_x = 18.226$ and $Q_y = 17.257$ respectively and $\Delta Q_{min} = 6.45 \times 10^{-3}$.

shows a comparison between the RDT's and $\overline{\mathbf{C}}$ matrix elements as derived in Eqs. (4.18) and (4.22). The RMS of the differences between the compared quantities are smaller than 10^{-6} thus numerically validating the relations.

Dependence on skew quadrupole strengths

The relations between $|\overline{\mathbf{C}}|$ and the RDT's are first order approximations. To investigate the accuracy of these relations, the mean of the ratio of the quantities compared in Fig. 4.1 are computed for increasing skew quadrupole strengths. The horizontal and vertical tunes are fixed at $Q_x = 18.226$ and $Q_y = 17.232$ respectively. Fig. 4.2 shows a plot of this mean ratio along with the standard deviation of the ratio as a function of closest tune approach (ΔQ_{min}) produced by the three skew quadrupoles. For this particular case, the quantities compared agree in the percent level for a ΔQ_{min} lower than 3×10^{-3} .

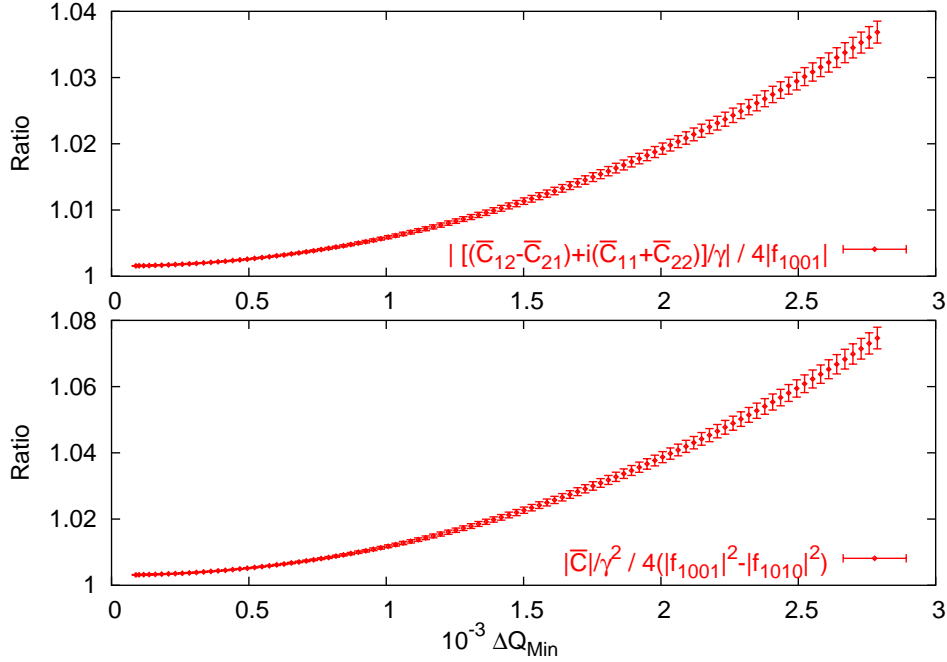


Figure 4.2: Top: Mean of the ratio of $|[(\overline{C}_{12} - \overline{C}_{21}) + i(\overline{C}_{11} + \overline{C}_{22})]/\gamma|$ and $4|f_{1001}|$. Bottom: Mean of the ratio of $|\overline{\mathbf{C}}|/\gamma^2$ and $4(|f_{1001}|^2 - |f_{1010}|^2)$. The error bars represent the standard deviation of the ratio of the respective quantities. The horizontal and vertical tunes are $Q_x = 18.226$ and $Q_y = 17.232$ and $\Delta Q_{min} = 6.45 \times 10^{-3}$.

Stop-Band Limits

To explore the behavior of Eq. (4.22), a scan of horizontal tune (Q_x) is performed with the vertical tune fixed at $Q_y = 0.228$. Fig. 4.3 shows the driving terms, $|f_{1001}|^2$ and $|f_{1010}|^2$ as well as $|\overline{\mathbf{C}}|/\gamma^2$ plotted as a function Q_x for the FODO lattice described above. The dominance of f_{1001} or f_{1010} is seen in Fig. 4.3 depending on the proximity to either the difference or sum resonance respectively. This transition is also evident from the behavior of

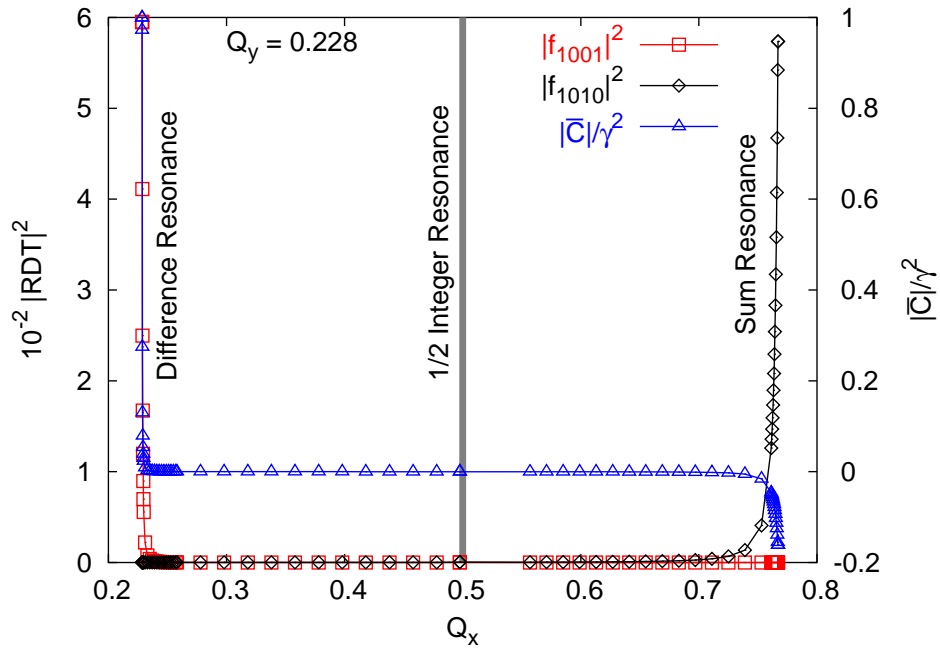


Figure 4.3: $|f_{1001}|^2$, $|f_{1010}|^2$ and $|\overline{\mathbf{C}}|/\gamma^2$ plotted as a function of Q_x ($Q_y = 0.228$). The stop-bands at the sum and the difference resonance show the dramatic increase in these functions. 1/2 integer resonance line is plotted as a reference.

$|\overline{\mathbf{C}}|/\gamma^2$ as it switches sign when we move from difference to the sum resonance in accordance with Eq. (4.22). There are missing data points at $Q_x = 0.5$ due to the 1/2 integer resonance.

4.3 Determinant of $\overline{\mathbf{C}}$

It has been demonstrated that \overline{C}_{12}/γ , \overline{C}_{11}/γ , \overline{C}_{22}/γ are measured using turn-by-turn data from beam position monitors (BPMs) [44, 45]. From \overline{C}_{12}/γ , one relies on fitting techniques to determine the location of coupler and estimate its strength to correct local coupling [44, 50]. However, the $|\overline{\mathbf{C}}|$ like the RDT's is a constant in coupler free regions and exhibits abrupt jumps at the locations of couplers. These discontinuities are intuitive and can be identified simply by visual inspection to the nearest BPM as seen in Fig. 4.1. The $|\overline{\mathbf{C}}|$ also allows one to easily estimate global quantities like ΔQ_{min} and local quantities like the strength and polarity of the coupler which are useful during machine operation. However, it will be seen that \overline{C}_{12}/γ has a better signal-to-noise ratio. Additionally it has better resolution to locate an isolated coupler more accurately using appropriate fitting techniques, while $|\overline{\mathbf{C}}|$ has a resolution to within a region between the two nearest BPMs.

To calculate the determinant, we propose a method to calculate \overline{C}_{21} given \overline{C}_{12} , \overline{C}_{11} , and \overline{C}_{22} at two locations with an arbitrary phase advance in both normal modes. Given two locations (1) and (2) in a coupler free region, $\overline{C}_{21}^{(1)}$ is given (see appendix C.3) by,

$$\begin{aligned} \overline{C}_{21}^{(1)} = & \left(-\overline{C}_{11}^{(1)} \cos \phi_a \sin \phi_b + \overline{C}_{12}^{(1)} \cos \phi_a \sin \phi_b \right. \\ & \left. + \overline{C}_{22}^{(1)} \sin \phi_a \cos \phi_b - \overline{C}_{12}^{(2)} \right) / (\sin \phi_a \sin \phi_b) \end{aligned} \quad (4.26)$$

where ϕ_a and ϕ_b are the phase advances between the two observation locations of the normal modes. We will demonstrate the effectiveness of such a calculation in a simple FODO lattice as well as in a complicated lattice such as RHIC where the coupling sources are mainly localized in the interaction regions with little or no coupling in the arcs.

It is also important to note that RDT's calculated using FFT techniques in [46] can be extended to compute $\overline{\mathbf{C}}$ matrix and hence the determinant according to Eqs. (4.20)- (4.24). The approach of N -turn map presented in [48] could also be extended to calculate both γ and $|\overline{\mathbf{C}}|$.

4.3.1 Calculation of \overline{C}_{12}/γ using SVD

An extension to the SVD based technique described in chapter 2 is used to infer the eigenmodes (a and b) of the beam. The knowledge of beam oscillations in ' $a - b$ ' plane can be used to calculate the $|\overline{\mathbf{C}}|$ matrix. This technique is briefly introduced to show the computation of $\overline{\mathbf{C}}$ matrix and its determinant.

A more detailed discussion can be found in Ref. [45, 52]. The betatron motion observed in the BPMs ($x - y$) plane can be expressed as

$$x_a = \sqrt{2J_a\beta_a\gamma} \cos(\phi_a + \psi_a) \quad (4.27)$$

$$x_b = \sqrt{2J_b\beta_b} c_b \cos(\phi_b + \psi_b + \Delta\psi_b) \quad (4.28)$$

and corresponding motion in the y plane ($x \rightarrow y, a \rightarrow b$). Here, $J_{a,b}$ and $\phi_{a,b}$ are the action and angle variables. $\beta_{a,b}$ and $\psi_{a,b}$ are the Twiss functions and $c_{a,b}$ and $\Delta\psi_{a,b}$ are related to the coupling matrix

$$c_{a,b} = \sqrt{C_{22,11}^2 + C_{12}^2} \quad (4.29)$$

$$\Delta\psi_{a,b} = \mp \arctan\left(\frac{C_{12}}{C_{22,11}}\right) \quad (4.30)$$

A data matrix $[B_x, B_y]$ consisting of t columns of turn-by-turn data at all BPM is decomposed using SVD [53] given by

$$\mathbf{B} = \hat{\mathbf{U}}\mathbf{\Sigma}\hat{\mathbf{V}}^T \quad (4.31)$$

Assume that the beam motion is dominated by betatron oscillations with transverse coupling. The SVD modes do not directly yield the eigenmodes of beam as in the case of uncoupled motion. However, the rank of the matrix is equal to the rank of sum of the physical eigenmodes. Therefore the SVD modes are simply linear combinations of the eigenmodes. A 4×4 orthogonal rotation matrix O is sufficient to transform the SVD modes into the eigenmodes. The inner product of two vectors

$$\langle \cos(\omega_m t), \cos(\omega_n t) \rangle = 0, \quad m \neq n \quad (4.32)$$

$$\langle \sin(\omega_m t), \sin(\omega_n t) \rangle = 0, \quad m \neq n. \quad (4.33)$$

Therefore, the knowledge of the Fourier spectrum from the “x-y” planes allows us to numerically compute the rotation matrix via projecting the sine-cosine terms at respective tunes onto the corresponding SVD modes

$$O = S\hat{V}^T \left(\sqrt{\bar{J}^*} V^T \right) \quad (4.34)$$

where “*” represents the operation of a transpose, pseudo-inverse, and a transpose. For small mixing of SVD modes, the rotation matrix can be constructed using linearized infinitesimal rotations prescribed in Ref. [52]

$$O = I + \sum \theta_{ij} L_{ij} \quad (4.35)$$

where θ_{ij} are the rotation angles and

$$L_{ij} = (\delta_{ik}\delta_{jl} - \delta_{il}\delta_{jk}); \quad \{k, l = 1 \dots 4\}. \quad (4.36)$$

A geometric view of constructing the rotation matrix in the phase space of spatial vectors is shown in Appendix B.

Using the rotation matrix, the normal modes are reconstructed from SVD modes as

$$\mathbf{O}^T \mathbf{S} \hat{\mathbf{V}}^T = \begin{pmatrix} \sqrt{\bar{J}_a \beta_a} \gamma \cos(\psi_a - \psi_a^0), & \sqrt{\bar{J}_a \beta_b} c_b \cos(\psi_a + \psi_{cb} - \psi_a^0) \\ \sqrt{\bar{J}_a \beta_a} \gamma \sin(\psi_a - \psi_a^0), & \sqrt{\bar{J}_a \beta_b} c_b \sin(\psi_a + \psi_{cb} - \psi_a^0) \\ \sqrt{\bar{J}_b \beta_a} c_a \cos(\psi_b + \psi_{ca} - \psi_b^0), & \sqrt{\bar{J}_b \beta_b} \gamma \cos(\psi_b - \psi_b^0) \\ \sqrt{\bar{J}_b \beta_a} c_a \sin(\psi_b + \psi_{ca} - \psi_b^0), & \sqrt{\bar{J}_b \beta_b} \gamma \sin(\psi_b - \psi_b^0) \end{pmatrix} \quad (4.37)$$

and the corresponding temporal vectors $\hat{\mathbf{U}}\mathbf{O}$. Note that the matrix $\mathbf{O}^T \mathbf{S} \hat{\mathbf{V}}^T$ is a $4 \times 2m$ matrix where m is the number of BPMs in each plane. Using the computed eigenvectors, \bar{C}_{12}/γ can be determined as

$$\frac{\bar{C}_{12}}{\gamma} = \text{sgn}(\sin \Delta\psi_a) \sqrt{\frac{\tilde{A}_a \tilde{A}_b}{A_a A_b}} \sin \Delta\psi_a \sin \Delta\psi_b. \quad (4.38)$$

Here $A_{a,b}^2 \equiv \bar{J}_{a,b} \beta_{a,b} \gamma^2$ and $\tilde{A}_{a,b}^2 \equiv \bar{J}_{a,b} \beta_{b,a} c_{a,b}^2$, where $\bar{J}_{a,b}$ are the average actions. Therefore,

$$\frac{\bar{C}_{11}}{\gamma} = \frac{\bar{C}_{12}}{\gamma} \cot \Delta\psi_b \quad (4.39)$$

$$\frac{\bar{C}_{22}}{\gamma} = -\frac{\bar{C}_{12}}{\gamma} \cot \Delta\psi_a \quad (4.40)$$

4.3.2 Calculation of $|\bar{C}|/\gamma^2$ from Tracking Data

Using Eqs. (4.26), (4.38), (4.39), and (4.40), $|\bar{C}|/\gamma^2$ can now be calculated from turn-by-turn BPM data. Single-particle tracking is performed using MAD-X on the FODO lattice described earlier to generate turn-by-turn data at a large number of BPM locations. For all simulations, we assume dual plane BPMs capable of measuring transverse positions in both planes, unless otherwise mentioned. The location of BPMs (1) and (2) in Eq. 4.26 to calculate \bar{C}_{21}/γ is arbitrary and only requires that there are no coupling sources present between them. For the purpose of the simulations BPM (2) is chosen to be the next upstream detector from location (1). Fig. 4.4 shows

a comparison of MAD-X model and SVD computed values of $|\overline{\mathbf{C}}|/\gamma^2$. The overall discrepancy is smaller than 0.01% and increases up to 1% in the coupler regions. To minimize the discrepancy in the coupler region, $\overline{\mathbf{C}}_{21}/\gamma$ at the BPM location just before the coupler, can be calculated using the previous BPM (downstream) instead of the BPM upstream. This maintains the region between the two BPMs to be coupler free and the calculation of $\overline{\mathbf{C}}_{21}/\gamma$ exact.

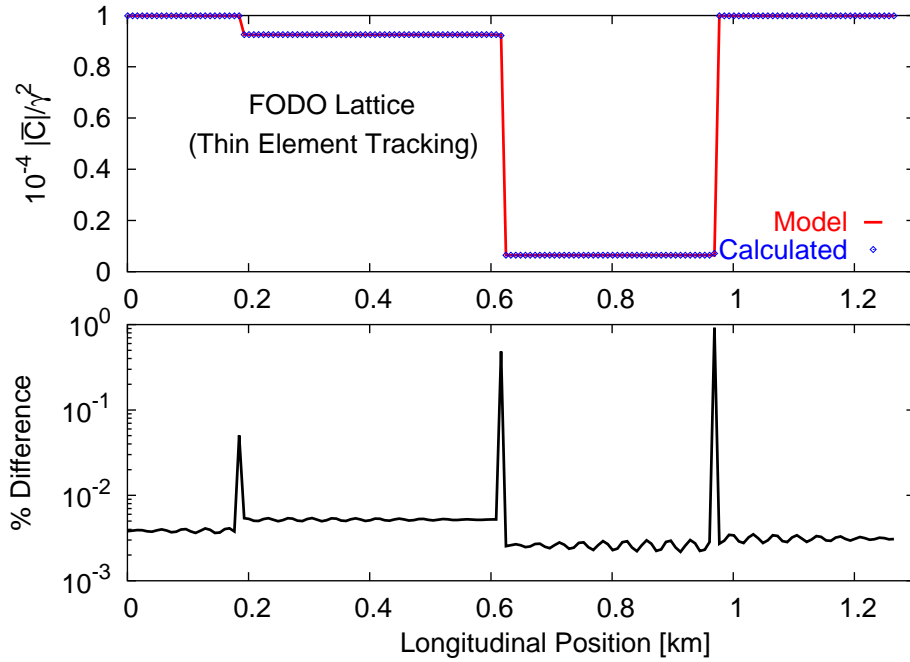


Figure 4.4: Top: Comparison of $|C|/\gamma^2$ between MAD-X model and SVD computed values from tracking data. Bottom: Difference between model and calculated values of $|C|/\gamma^2$. Horizontal and vertical design tunes are $Q_x = 18.226$ and $Q_y = 17.257$ respectively and $\Delta Q_{min} = 6.45 \times 10^{-3}$.

To investigate the effect of noise in BPMs, different levels of Gaussian noise were introduced into turn-by-turn tracking data used to compute $\overline{\mathbf{C}}$ matrix. Fig. 4.5 shows the normalized RMS of the difference for $|C|/\gamma^2$ and $\overline{\mathbf{C}}$ matrix elements between model and calculated values as a function of $\sigma_{noise}/\text{signal}$ amplitude. It is clear that noise deteriorates the measurements. We observe that $\overline{\mathbf{C}}_{12}/\gamma$ is more robust against noise than the other elements of the \mathbf{C} matrix. The discrepancy of the effect of noise between $\overline{\mathbf{C}}_{12}/\gamma$ and $\overline{\mathbf{C}}_{11}$ can be attributed to the calculation of $\Delta\psi_{b,a}$ and is under study. $\overline{\mathbf{C}}_{21}/\gamma$ inherently has large errors since Eq. 4.26 is only exact in a coupler free region. This

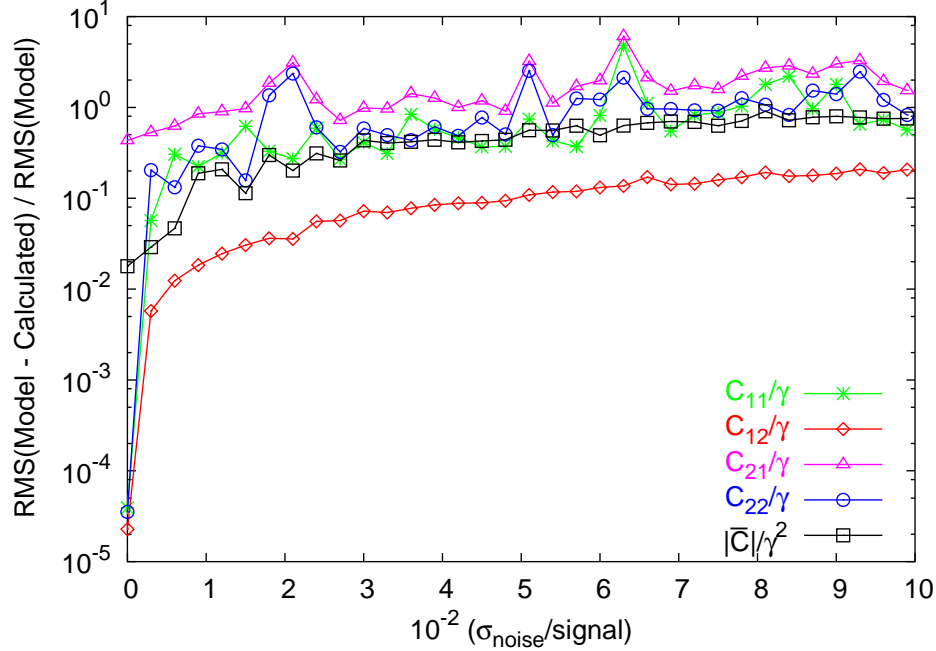


Figure 4.5: Normalized RMS of the difference of $|C|/\gamma^2$ between MAD-X model and SVD computed values for increasing amount of Gaussian noise in turn-by-turn data. Horizontal and vertical tunes are $Q_x = 18.226$ and $Q_y = 17.257$ respectively and $\Delta Q_{min} = 6.45 \times 10^{-3}$.

can be improved by the choice of appropriate BPMs for the calculation as explained above. It was shown that the choice of number of turns in tracking affects the computation of \overline{C} matrix due to the periodicity effect caused by the number of significant digits in the tune [45]. In real data $\overline{C}_{11}^{\prime}$ unlike \overline{C}_{12}/γ were shown to be susceptible to large errors due to signal “leaks” in BPMs and their corresponding electronics [43, 50].

4.3.3 Calculation of $|\overline{C}|/\gamma^2$ for RHIC Lattice

Single particle tracking using the RHIC lattice was performed to verify the applicability of this approach for a more realistic operating accelerator with several coupling sources. RHIC consists of two three-fold symmetric rings with six interaction regions. Each arc is made of 11 FODO cells with 80° phase advance, and interaction regions consist of almost the same FODO cells without the dipoles [54]. A model of RHIC containing realistic but uncorrected

errors is used to track a single particle for 2000 turns with $Q_x = 28.266$ and $Q_y = 29.212$. The ΔQ_{min} for this lattice is 4.37×10^{-2} . Fig. 4.6 shows a calculation of $|\overline{C}|/\gamma^2$ from turn-by-turn data compared to model values from MAD-X. One can clearly see that the coupling sources (for example rolled quadrupoles) are quite strong and mainly located in interaction regions. The

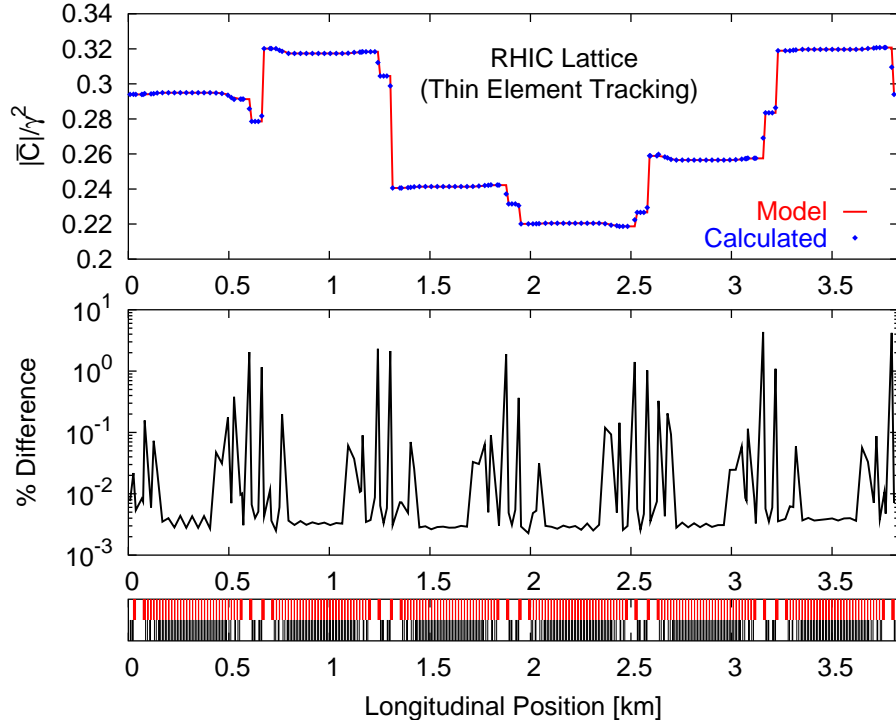


Figure 4.6: Top: Comparison of $|\overline{C}|/\gamma^2$ between MAD-X model and SVD computed values from tracking data. Middle: Difference between model and calculated values of $|\overline{C}|/\gamma^2$. Bottom: A representation of the lattice (dipoles in black and quadrupoles in red) is shown in the bottom graph. The horizontal and vertical tunes were $Q_x = 28.266$ and $Q_y = 29.212$ respectively and $\Delta Q_{min} = 4.37 \times 10^{-2}$.

agreement between model and calculated values of $|\overline{C}|/\gamma^2$ is better in the arcs than in the interaction regions (IR's). The larger discrepancies arising in the IR's are due to the presence of strong coupling sources. However, even in a complicated lattice like RHIC, the sources are clearly identified and errors in $|\overline{C}|/\gamma^2$ are below 5 %.

For the above simulation, we assumed dual plane BPMs in the lattice. However, this is not true for RHIC and most operating hadron colliders. RHIC

consists of 160 BPMs per plane per ring: 72 dual-plane BPMs distributed through the IR's, and 176 single-plane BPMs distributed in the arcs capable of acquiring 1024 turns. The single plane BPMs in RHIC are confined to the arc regions where coupling sources are minimal. A more sophisticated algorithm to estimate $|\overline{\mathbf{C}}|/\gamma^2$ with lattices consisting of both single and double plane BPMs is under investigation. In real accelerators, many BPMs routinely fail resulting in unreliable data. It has been shown that preprocessing of BPM data is usually effective in removing faulty BPMs and maintain data integrity [55] to obtain reliable measurements.

4.3.4 Calculation of skew quadrupole strengths

In [56] and [57] a method to obtain multipole strengths from the measurement of RDT's was proposed. Skew quadrupole strengths are equivalently obtained from the measurement of the $\overline{\mathbf{C}}$ matrix by use of the above relations. According to fig. 4.7 we assume that only one skew quadrupole of integrated

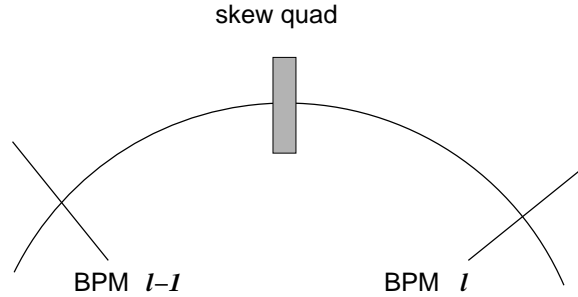


Figure 4.7: Schematic view of a skew quad and the neighbor BPMs

strength k exists between the two BPMs where the $\overline{\mathbf{C}}$ matrices have been measured. From [56] and [57] the integrated strength \bar{k} is given by:

$$\begin{aligned} \bar{k} = & -4e^{-i(\phi_x^{skew} - \phi_y^{skew})} \\ & \times \left(f_{1001}^{(l)} e^{i(\phi_x^l - \phi_y^l)} - f_{1001}^{(l-1)} e^{i(\phi_x^{l-1} - \phi_y^{l-1})} \right), \end{aligned} \quad (4.41)$$

with $\bar{k} = k\sqrt{\beta_x^{skew}\beta_y^{skew}}$. Here k is the strength of coupler, $\beta_{x,y}^{skew}$ and $\phi_{x,y}^{skew}$ are the Twiss functions at the location of the skew quadrupole. $\phi_{x,y}^l$ and $\phi_{x,y}^{l-1}$ are the betatron phases at the l^{th} and $(l-1)^{th}$ BPMs respectively and $f_{1001}^{(l)}$ and $f_{1001}^{(l-1)}$ are the corresponding RDT's. These terms are given by Eq. (4.18) as a function of the measured $\overline{\mathbf{C}}$ matrix. The RDT f_{1010} can also be used

leading to a similar equation. It is also interesting to relate the change of the determinant of $\overline{\mathbf{C}}$ to the strength of the skew quadrupole. By manipulating the above expressions (see alternate derivation in appendix C.4),

$$\bar{k} = -\frac{1}{\chi} \left(\frac{|C^{(l)}|}{\gamma^{(l)^2}} - \frac{|C^{(l-1)}|}{\gamma^{(l-1)^2}} \right), \quad (4.42)$$

where χ is given by

$$\begin{aligned} \chi = \frac{1}{\gamma^{(l)}} & \left(-\sin \delta\phi_x \sin \delta\phi_y \overline{C}_{21}^{(l)} + \cos \delta\phi_x \cos \delta\phi_y \overline{C}_{12}^{(l)} \right. \\ & \left. + \sin \delta\phi_x \cos \delta\phi_y \overline{C}_{22}^{(l)} - \cos \delta\phi_x \sin \delta\phi_y \overline{C}_{11}^{(l)} \right), \end{aligned} \quad (4.43)$$

where $\delta\phi_{x,y} = \phi_{x,y}^{skew} - \phi_{x,y}^l$ are the phase advances between the skew quadrupole and the second location of observation. Using Eq. (C.7), Eq. (4.43) can also be expressed as

$$\chi = \frac{C_{12}^{skew}}{\gamma^l} \quad (4.44)$$

To determine the applicability of the above expressions, a simulation using strongly coupled RHIC lattice is performed. The ΔQ_{min} for this lattice is 4.37×10^{-2} . Fig. 4.8 shows skew quadrupole strengths determined from Eq. (4.42) for the RHIC lattice. The presence of large coupling sources lead to relative errors of calculated strengths in the 20% level. This is due to fact that these expressions are first order approximations, and deviate with large coupling as illustrated in section 4.2.4.

4.4 The closest tune approach

The following expression relating the closest tune approach and the determinant of $\overline{\mathbf{C}}$ is given in [47] and [48],

$$\Delta Q_{min} = \frac{2\gamma(\cos 2\pi Q_x - \cos 2\pi Q_y)}{\pi(\sin 2\pi Q_x + \sin 2\pi Q_y)} \sqrt{|\overline{\mathbf{C}}|}. \quad (4.45)$$

This equation cannot hold true in general since its l.h.s. is invariant around the ring but the r.h.s. is not, as explained in section 4.2.3. Only close to the difference resonance the determinant of $\overline{\mathbf{C}}$ tends to be invariant and Eq. (4.45)

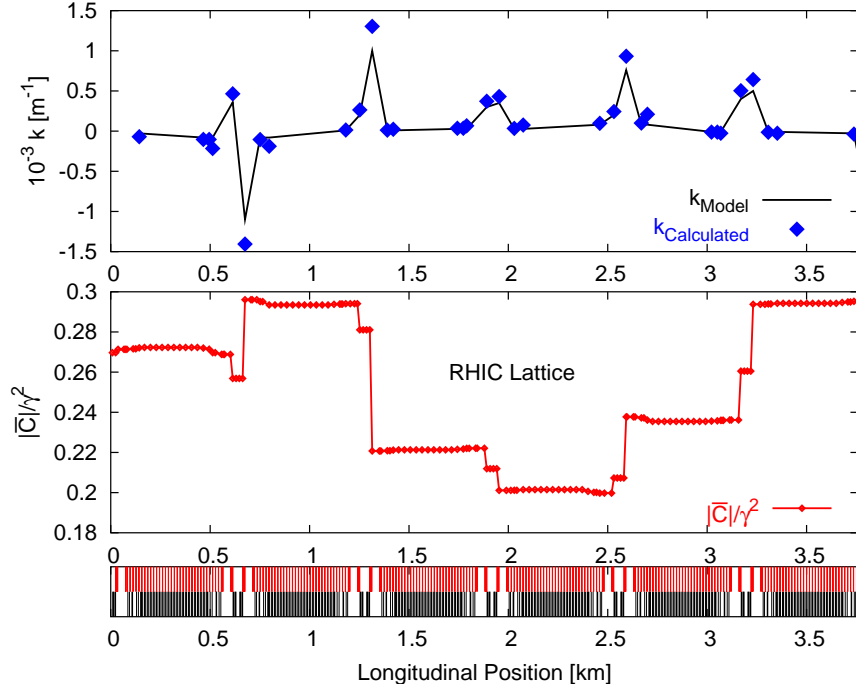


Figure 4.8: Top: Skew quadrupole strengths calculated from RDT's and \overline{C} matrix are compared to MAD-X model values. Note that RDT's are calculated from \overline{C} matrix using Eqs. (4.18) and (4.19). Middle: $|\overline{C}|/\gamma^2$ is plotted as a function of longitudinal position. A representation of the lattice (dipoles in black and quadrupoles in red) is shown in the bottom graph. The horizontal and vertical tunes are $Q_x = 28.266$ and $Q_y = 29.212$ respectively and $\Delta Q_{min} = 4.37 \times 10^{-2}$.

is considered to be a good approximation. Under this assumption the closest tune approach can also be related to the resonance terms,

$$\Delta Q_{min} = \frac{\cos 2\pi Q_x - \cos 2\pi Q_y}{\pi(\sin 2\pi Q_x + \sin 2\pi Q_y)} \times \left(\frac{4\sqrt{|f_{1001}|^2 - |f_{1010}|^2}}{1 + 4(|f_{1001}|^2 - |f_{1010}|^2)} \right) \quad (4.46)$$

and since we assume the tunes to be close to the difference resonance the approximation $|f_{1001}| \gg |f_{1010}|$ might also be used [47, 48]. A computer simulation is performed to investigate the validity of Eqs. (4.45) and (4.46). The same FODO lattice with three skew quadrupoles were used with horizontal

and vertical tunes $Q_x = 18.226$ and $Q_y = 17.239$ respectively. Since $|\overline{\mathbf{C}}|$ varies around the ring, ΔQ_{min} is calculated with the three values of $|\overline{\mathbf{C}}|$ at the three locations of skew quadrupoles and plotted as a function of increasing skew quadrupole strengths as shown in Fig. 4.9. We observe a dispersion in the

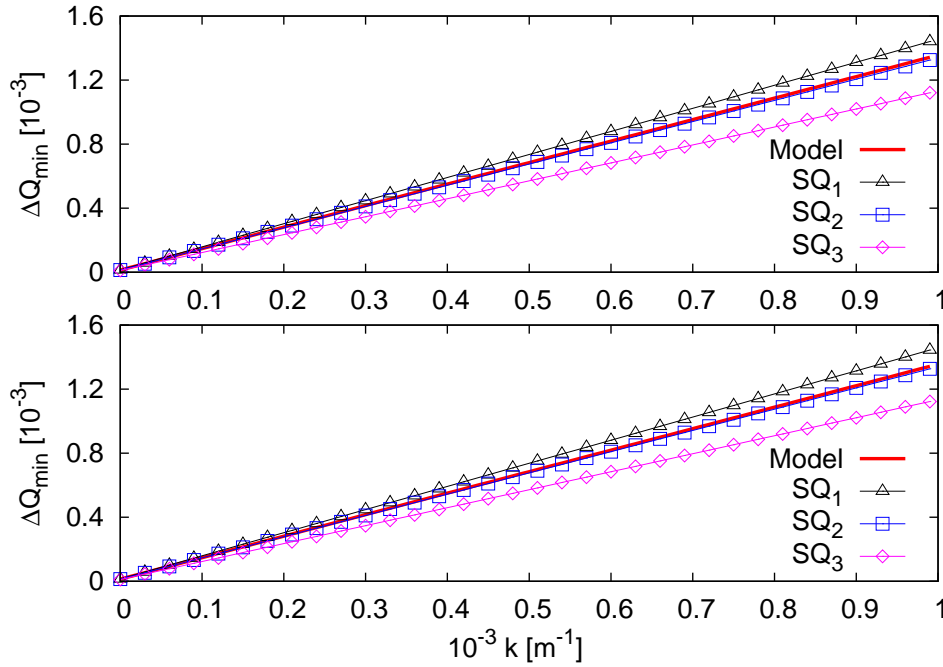


Figure 4.9: Top: ΔQ_{min} calculated using the three different values of RDT's at respective locations of skew quadrupoles as a function of their strength. Bottom: ΔQ_{min} calculated using three different values of $|\overline{\mathbf{C}}|$ at respective locations of skew quadrupoles as a function of their strength ($Q_x = 18.226$, $Q_y = 17.239$).

ΔQ_{min} curves depending on choice of the $|\overline{\mathbf{C}}|$ value used to calculate ΔQ_{min} . If the tunes are closer to the coupling resonance, the relative longitudinal variation in $|\overline{\mathbf{C}}|$ around the ring is smaller, hence reducing this dispersion.

4.5 Conclusions

Direct relations are established between the coupling matrix and the RDT's. This allows reinterpretation of the coupling matrix in terms of resonances and using results from both formalisms indistinctly. Numerical simulations are car-

ried out to confirm these relations and explore their scope of application to real accelerators. The determinant of $\overline{\mathbf{C}}$ and the RDT's (f_{1001}^{1010}) have been demonstrated to exhibit distinct behavior that unambiguously reveals the region of the coupling sources.

A new approach to compute the full $\overline{\mathbf{C}}$ matrix and hence the determinant from turn-by-turn data is presented and comparison to model shows excellent agreement. An approach to extract the skew quadrupole strengths previously using RDT's is also extended to $\overline{\mathbf{C}}$ matrix. The applicability of the expression for ΔQ_{min} from the $|\overline{\mathbf{C}}|$ has been discussed.